Solid Earth Discuss., 7, 2663–2695, 2015
www.solid-earth-discuss.net/7/2663/2015/
doi:10.5194/sed-7-2663-2015

Solid Earth Discussions
Open Access

Strain localization in ultramylonitic marbles by simultaneous activation of dislocation motion and grain boundary sliding (Syros, Greece)

A. Rogowitz[1,2], **J. C. White**[3], **and B. Grasemann**[1]

[1]Department for Geodynamics and Sedimentology, University of Vienna, Althanstrasse 14, 1090 Vienna, Austria
[2]Natural History Museum, Burgring 7, 1010 Vienna, Austria
[3]Department of Earth Sciences, University of New Brunswick, 3 Bailey Dr, Fredericton, NB E3B 5A3, Canada

Received: 9 August 2015 – Accepted: 22 August 2015 – Published: 18 September 2015

Correspondence to: A. Rogowitz (anna.rogowitz@univie.ac.at)

Published by Copernicus Publications on behalf of the European Geosciences Union.

Abstract

Extreme strain localization occurred in the center of the cross-cutting element of a flanking structure in almost pure calcite marbles from Syros, Greece. At the maximum displacement of 120 cm along the cross-cutting element evidence of grain size sensitive deformation mechanisms can be found in the ultramylonitic marbles, which are characterized by (1) an extremely small grain size (~ 3 µm), (2) grain boundary triple junctions with nearly 120° angles, (3) a weak crystallographic preferred orientation with very low texture index (J = 1.4), (4) a random misorientation angle distribution curve and (5) the presence of small cavities. Using transmission electron microscopy a deformation sequence is observed comprising, first recrystallization by bulging resulting in the development of the fine-grained ultramylonite followed by the evolution of a high dislocation density (~ 10^{13} m^{-2}) with ongoing deformation of the fine-grained ultramylonite. The arrangement of dislocations in the extremely fine grain sized calcite differs from microstructures created by classical dislocation creep mediated by combined glide and thermally activated climb. Instead, it exhibits extensive glide and dislocation networks characteristic of recovery accommodated by cross-slip and network-assisted dislocation movement without formation of idealized subgrain walls. The enabling of grain boundary sliding to dislocation activity is deemed central to initiating and sustaining strain softening and is argued to be an important strain localization process in calcite rocks, even at high strain rate (10^{-9} s^{-1}) and low temperature (300 °C).

1 Introduction

Strain localization in monomineralic rocks when associated with brittle precursors, can exhibit microstructural evolution comprising grain size reduction, and ensuing activation of grain-size-sensitive (GSS) deformation mechanism such as diffusion creep, cataclastic flow and independent grain boundary sliding (GBS) (Schmid, 1976; Schmid et al., 1977; Etheridge and Wilkie, 1979; Segall and Pollard, 1983; Pennacchioni and

SED
7, 2663–2695, 2015

Mancktelow, 2007; Menegon et al., 2013). The aforementioned mechanisms are typically observed and/or anticipated to result in a random crystallographic orientation or decrease in the intensity of any pre-existing texture formed during plastic deformation of the original material. However, reports of fine-grained deformed polycrystalline materials showing a crystallographic preferred orientation (CPO) indicate that operation of deformation mechanisms during GBS can result in the development of a CPO (Schmid et al., 1977; Rutter et al., 1994; Sundberg and Cooper, 2008; Wang et al., 2010; Hansen et al., 2011; Kushnir et al., 2015).

GBS is a GSS flow behaviour able to support extremely high strains; nevertheless, accommodation of relative grain displacement requires accommodation mechanisms to occur collaboratively in order to maintain strain compatibility. Most commonly, diffusional (Coble) creep, dissolution-precipitation creep, dislocation glide and climb within the grain boundary and the grain boundary region are invoked (Gifkins, 1976). More recently the simultaneous activity of classical dislocation creep and GBS has been reported to be active in ultramylonites deformed at high temperatures (Wang et al., 2010).

In this contribution, we present observations from an essentially pure calcite marble layer from Syros (Cyclades, Greece) deformed under lower greenschist facies conditions (Rogowitz et al., 2014). In these rocks, a flanking structure (Fig. 1; Passchier, 2001; Grasemann and Stüwe, 2001) has formed in the presence of a crack (i.e. cross-cutting element) that rotated during top-to-the-east shear. At the location of maximum displacement (120 cm) along the cross-cutting element the marble is extremely fine grained ($\sim 3\,\mu m$) within the range for which deformation by GSS mechanisms are anticipated. For the observed grain size and deformation conditions, maximum strain rates of $\sim 10^{-9}\,s^{-1}$ have been determined (Rogowitz et al., 2014). Therein lies a potential contradiction in that such strain rates at low temperatures point toward the operation of brittle deformation rather than ductile flow.

In this contribution we present and discuss the microstructure of the aforementioned ultramylonite. Detailed analyses have been performed using optical microscopy, sec-

SED
7, 2663–2695, 2015

ondary electron microscopy (SEM), electron backscatter diffraction (EBSD) mapping and transmission electron microscopy (TEM) in order to elucidate the deformation mechanisms active at the given temperature, differential stress and strain rate conditions associated with this extreme strain localization.

2 Geological setting and outcrop description

The ultramylonite in question developed during formation of an *a* type flanking structure in an almost pure calcite marble situated on Syros (UTM 35 414 840° N 313 839° E), which is one of the Cycladic Islands that are located in the back arc of the Hellenic subduction zone (Papanikolauo, 1987; Wortel et al., 1993). The Cycladic area has been, in general, affected by two main metamorphic events: (1) an Eocene eclogite-blueschist metamorphic event and (2) an oligo-Miocene greenschist-facies event (Jolivet and Brun, 2010 and references cited therein). The rocks exposed on Syros mainly belong to the Cycladic blueschist unit (CBU), which is dominated by metagabbros, metabasites, metasediments and schists. Petrological studies (e.g. Trotet et al., 2001; Keiter et al., 2004) constrain the pressure-temperature evolution of rocks on Syros to peak conditions on the order of 1.8 GPa and 550 °C. The greenschist facies overprint is assumed to encompass retrograde conditions around 300 °C and 2 to 4 kbar (Trotet et al., 2001; Keiter et al., 2004; Schumacher et al., 2008). There is a general increase in greenschist facies overprint towards the SW of Syros attended by a NE–SW stretching lineation and a predominant top-to-the-east sense of shear (Keiter et al., 2004; Philippon et al., 2011; Rogowitz et al., 2015).

The pre-existing crack (cross-cutting feature) associated with the flanking structure (Fig. 1a), is initially orientated at an angle of 90° to the main foliation. During greenschist facies overprinting, rotation of the crack produced an antithetic (top-to-the-west) shear zone (Fig. 1a). A maximum displacement of 120 cm occurs in the center of the shear zone where the initially coarse-grained, almost pure calcite marble has its grain size reduced to an extremely fine-grained ultramylonite (Fig. 2) with a porcelaneous

SED
7, 2663–2695, 2015

macroscopic appearance (Fig. 1b). The ultramylonitic layers have a total thickness of 0.12–0.48 cm and border the shear zone that comprises alternating protomylonitic and ultramylonitic calcite layers, having a total thickness of 1.5 cm (Rogowitz et al., 2014). Assuming that the marble deformed under simple shear conditions the total strain at this locality is at least 80. If it is assumed, that most of the strain was accommodated by the fine-grained ultramylonite, a shear strain up to 1000 can be inferred as an upper limit.

3 Methods

3.1 Sample preparation

The hand specimens of the shear zone were cut perpendicular to the shear-zone boundary and parallel to the stretching lineation (xz of finite strain). Mechanically polished thin-sections with a thickness between 20 and 30 µm were prepared for microstructure analysis. Thin sections selected for scanning electron microscopy (SEM) and electron backscattered diffraction (EBSD analyses were chemo-mechanically polished with an alkaline colloidal silica suspension (Köstrosol 3530; pH 9.2–10). To establish electric conductivity the thin sections were carbon coated. Additionally hand specimens have been broken in approximately an xz and xy orientation of finite strain for grain boundary surface analysis via SEM microscopy. Specimens for TEM have been prepared by the focused ion beam technique (FIB) and standard argon ion beam thinning using a Gatan precision ion polishing system (PIPS©).

In order to characterize microstructural development during progressive deformation of the fine-grained ultramylonitic layer, FIB-foils were prepared along a profile across small calcite grains within the transition zone between coarser grained marble and the fine-grained ultramylonite. This enabled comparison of the defect structure within newly developed grains and those that have been further deformed within the layer of focus. For analysis of microstructures within the ultramylonitic calcite FIB-foils showing

SED
7, 2663–2695, 2015

a profile over at least two grains have been prepared. PIPS was used to prepare specimens across comparable transitions in order to sample larger areas for comparison and integration with the FIB observations.

3.2 Microfabric analysis

A Leica DM4500 P optical microscope has been used for selecting appropriate thin sections for detailed microfabric analysis (Fig. 2). In order to visualize the presence of cracks, cavities and grain boundary surface character secondary electron microscopy has been performed on a FEI Quanta 3-D FEG SEM equipped with an EDAX Pegasus Apex 4 system consisting of a Digiview IV EBSD camera and an Apollo XV silicon drift detector for EDX-spectrometry at the University of Vienna, Department of Lithospheric Research (Figs. 3 and 5). Crystallographic orientations have been measured by combined electron backscatter diffraction (EBSD) mapping and EDX-spectrometry (Fig. 4). The instrument was operated at a 10 kV accelerating voltage, a 4 nA probe current at working distances between 10 and 14 mm. For EBSD analysis the sample has been tilted up to an angle of 70°.

EBSD data were processed using the MATLAB© toolbox for quantitative texture analysis MTEX (Bachmann et al., 2010). Orientation distribution functions (ODFs) were calculated after Bunge (1982). The orientation of the *c* (0001), *–a* ⟨11-20⟩, *r* {10-14}, *f* {01-12}, *e* {01-18} and *m* {10-10} poles were derived from the ODF and plotted as equal area lower hemisphere projections (Fig. 4a). Additionally, the misorientation-angle distributions for neighbour-pair and random-pair grains have been determined and are represented together with the calculated theoretical, random misorientation-angle distribution for trigonal crystal symmetry (Fig. 4b; Mackenzie and Thompson, 1957).

TEM was performed with a JEOL 2011 STEM equipped with a double-tilt analytical holder and a Gatan MSC digital camera for imaging at the University of New Brunswick, Microscopy and Microanalysis Facility. The TEM was operated at an accelerating voltage of 200 keV in bright- and dark-field modes (Figs. 6 and 7).

SED
7, 2663–2695, 2015

3.3 Dislocation density determination

Dislocation densities have been measured by use of the line-cut method. The number of intersections between dislocations and a prescribed grid of traverse lines has been counted. The dislocation density ρ was then determined using:

$$\rho = 2N/Lt, \quad (1)$$

with t being the specimen thickness, N the number of counted intersections and L the total length of the used grid.

32 random chosen TEM bright field images have been used in order to get a representative result. Dislocation densities have been calculated for an average, maximum and minimum specimen thickness (Table S1 in the Supplement).

4 Results

4.1 Microfabric

The Syros ultramylonitic marble is characterized by quasi-equigranular to low aspect ratio fine grained calcite (between 1 and 9 µm) with an average grain size of ~ 3 µm (Fig. 2). Grains show a pronounced shape preferred orientation (SPO) that is oblique to the main foliation, consistent with top-to-the-west non-coaxial displacement within the shear zone (Fig. 2b). Triple- and four-grain junctions occur throughout the ultramylonite. Rarer coarse relict grains appear to have more curved grain boundaries while small grains show crystal faces (Fig. 2c). Notably at the boundary in proximity to a coarser grained layer, a higher number of small bulges connected to coarser, curved calcite grains can be observed (Fig. 6a and b). Small cavities with a size up to 1 µm are located at grain-triple and four-grain junctions (Figs. 3a–d and 5c and d). Additionally small, elongated grain boundary openings preferentially orientated at grain boundaries inferred to have been in extension can be observed (Fig. 3e and f). Small

SED
7, 2663–2695, 2015

cracks orientated at approximately the same angle are observed to be concentrated at grain boundaries orientated with a high angle to the foliation (Figs. 3g and h and 5f).

Calcite grains in the ultramylonitic layers show a weak crystallographic preferred orientation (Fig. 4a; max. *J* index 1.4) with a *c* axis distribution around the periphery of the pole figure containing a point maximum orientated oblique to the foliation plane. The poles of *e* planes (01-18) show a similar preferred orientation to that of the *c* axis distribution. Both *a* axes ⟨11-20⟩ and poles of *m* planes {10-10} are preferentially orientated in a slightly oblique girdle with respect to the foliation plane, orientated almost perpendicular to the *c* axis point maximum, showing one point maximum in the center of the pole figure. The poles of *r* planes {10-14} show four (4) very weakly defined point maxima of which one is almost perpendicular to the foliation plane.

Misorientation-angle distributions (Fig. 4b) of neighbour-pair and random-pair grains are similar and reasonably track the calculated curve of an ideal random misorientation-angle distribution calculated for trigonal crystal symmetry. Minor variation in curves is visible for misorientations up to 40° where neighbour-pair grains constitute a higher population fraction and for misorientations higher than 80° for which the fraction of random-pair grains is higher.

Almost no internal misorientation is visible within the grains displayed as a misorientation deviation map wherein the misorientation over each grain with respect to its average misorientation is plotted (Fig. 4c). Small (< 10 µm) almost equigranular grains appear to be strain free or have a uniform strain distribution. only within coarser grains (> 10 µm) are misorientations up to 13° observed.

4.2 Grain surface microstructure

High resolution SEM secondary electron images (SEI) of broken specimens show that the marble preferentially fractures along grain boundaries having well-pronounced crystal faces (Fig. 5a and b); only grains larger than 15 µm break along cleavage planes during sample preparation. Similar to both SEI of thin sections (4.1) and TEM observations (4.3), cavities of varying sizes up to 1 µm across are preferentially located at grain

SED
7, 2663–2695, 2015

triple junctions (Fig. 5c and d). Locally grain boundary openings following more than one grain occur resulting in thin intergranular cracks (Fig. 5a) which might be a preparation artefact. Small ledges at grain boundaries seem to be often located close to a cavity or grain boundary opening (Fig. 5a and c). Small, similarly orientated cavities are concentrated at grain boundaries (Fig. 5f), as also observed in SE of thin sections. In general the grain surfaces are very smooth only rarely fine pores occur. These pores are varying slightly in size but seem to have a similar oval shape (Fig. 5e). Locally grain boundaries are slightly curved appearing to flow around neighbouring grains (Fig. 5e).

4.3 Defect microstructure (TEM)

A heterogeneous grain microstructure occurs across the optical transition zone (Fig. 6a and b). These variations correlate with distinctive defect substructures observed by TEM. Coarser calcite grains contain a high density number of low angle subgrain boundaries defined by well-arranged dislocations walls, as well as free dislocations (Fig. 6c and d). Smaller grains located in the transition zone are almost free of dislocations, showing a sharp, convex high-angle grain boundary towards the dislocation-rich coarser calcite grains (Fig. 6b–d). Locally small grains form pronounced crystal faces (Fig. 6d).

Grains within the fine-grained ultramylonite contain abundant free dislocations (Fig. 7). Dislocation multiplication by Frank–Read sources is observed throughout the ultramylonite at grain boundaries (Fig. 7a); likewise, glide dislocations are commonly concentrated or pinned at grain boundaries (Fig. 7b). Glide dislocations are well developed on *f* type planes (Fig. 7c and d). All grains independent of size have a high density of dislocations on the order of $10^{13}\,m^{-2}$ having an average density of $5 \times 10^{13}\,m^{-2}$ (Fig. 7e).

In contrast to the coarser grained calcite only rarely exhibit well-formed subgrain boundaries, Instead, dislocation networks define small cells of around 200 nm (Fig. 7f), in size, showing partly a hexagonal shape.

SED
7, 2663–2695, 2015

Voids are conspicuous within the ultramylonite at grain triple junctions and as arrays along grain boundaries consistent with SEM observations.

5 Analysis and discussion

The Syros ultramylonite exhibits distinctive attributes whose origin should have an internally consistent explanation. These are: (1) extreme grain size reduction at low homologous temperature during the greenschist deformation; (2) high-strain deformation of the resultant ultrafine-grained calcite; (3) intense dislocation glide as a component of the high strain concomitant with; (4) the formation of nanopores; and (5) creation of a primary CPO in the ultrafine-grained calcite. It is argued that these collectively demonstrate intense plastic deformation transitioning to deformation by dislocation-accommodated GBS.

5.1 Grain size reduction

Extreme reduction in grain size can occur by brittle/frictional deformation (Blenkinsop, 1991; Mair and Abe, 2011) or solid-state dynamic recrystallization (Harwick et al., 1961; White, 1973, 1977; Poirier and Nicolas, 1975; Guillopé and Poirier, 1979; Etheridge and Wilkie, 1979, 1981; White, 1982; Handy et al., 2007; Sakai et al., 2014 amongst others). Although brittle fractures commonly act as loci for subsequent ductile displacement, there is no indication of this behaviour for the ultramylonite. The microstructural evolution clearly demonstrates that dynamic rerystallization during intense plastic deformation is the grain size reducing mechanism (Rogowitz et al., 2014). Small calcite grains within the transition zone between the two ultramylonitic layers of contrasting grain size have low dislocation densities compared to adjacent coarser grains (Fig. 6c and d). The convex curvature of the grain boundary towards highly dislocated grains indicates grain boundary migration from the small grain towards the coarser grain. The latter is indicative of bulging recrystallization where the driving force for grain boundary movement

SED
7, 2663–2695, 2015

is the contrast in internal strain energy between grains (Takeuchi and Argon, 1976; White and White, 1980; Sakai and Jonas, 1984; Platt and Behr, 2011). During grain boundary migration, the dislocation-rich volume is reorganized (consumed) resulting in a decrease in elastic strain energy. The ensuing small grain size favours a GSS constitutive behaviour (e.g. Gifkins, 1976; Schmid et al., 1977; Etheridge and Wilkie, 1979; White et al., 1980; Rutter and Brodie, 2004).

5.2 Differential stress determination

Differential stress ultramylonite deformation has been calculated using dislocation density and recrystallized grain size. The theoretical relation between dislocation density and stress has been used to get estimation on flow stress conditions σ (Kohlstedt and Weathers, 1980):

$$\sigma = \alpha\mu\rho^{0.5}, \quad (2)$$

Where α is a constant depending on the type of dislocation, μ is the shear modulus and b is the Burgers vector length. Calculations used $\alpha = 1$ and $\mu = 28.9$ GPa (for calcite at 300 °C; Dandekar, 1968). Values for the Burgers vector length vary depending on the chosen slip plane (4.98, 6.37, and 8.09 Å) depending on the chosen glide system (Goetze and Kohlstedt, 1977). Flow stresses have been calculated using dislocation densities ρ calculated for maximum, minimum and average specimen thickness. Additionally the experimental calibration of De Bresser (1996) linking flow stress and dislocation density has been used:

$$\sigma = 10^{-6.21}\rho^{0.62}. \quad (3)$$

Although this calibration is based on results from single crystals it is assumed to fit for polycrystalline material deformed at higher differential stresses (> 40 MPa). The results obtained for average dislocation densities can be found in Table S1. The calculated differential stress varies depending on the chosen active glide system and therefore the

SED
7, 2663–2695, 2015

Burgers vector length (Table S1, Fig. 8). For basal slip as the dominant glide system the stress for an average specimen thickness ranges between 64 and 110 MPa, for preferred *f* slip differential stresses reach values between 82 and 140 MPa, Burgers vector length observed to be active for *r* and *f* slip results in stresses between 104 and 178 MPa. Using the experimental ρ–σ calibration of De Bresser (1996) even higher stresses are reached ranging between 133 and 260 MPa (Table S1, Fig. 8).

Differential stress calculated with the paleowattmeter (Austin and Evans, 2009) and paleopiezometer of Schmid (1980) lie in a range between 200 and 170 MPa (Figs. 8 and 9). These values are close to the average stresses calculated for *r* and *f* slip as well as average stresses calculated with the equation of De Bresser (1996; Fig. 8).

Differential stress values calculated by the different methods (paleowattmeter, paleopiezometer, dislocation density) result in different values that nevertheless all lie in the same order of magnitude. Differential stresses obtained by relations between grain size and stress lie between 170 and 200 MPa and seem to be the most accurate ones, taking into account that at these conditions both the paleowattmeter and paleopiezometer are consistent with the field boundary theory. For stresses calculated in relation to the dislocation density we are only going to discuss values corresponding to an average specimen thickness. Using the theoretical relation by Kohlstedt and Weathers (1980) we get three different average values, depending on the burgers vector length. The stress calculated for a burgers vector with a length of 4.98 Å, as observed for basal slip is in average 88 MPa. This relatively small value would correspond to deformation at lower strain rates and plot in the deformation mechanism map completely within the GSS creep field what seems unlikely taking the observed simultaneous activation of GBS and dislocation movement into account. Also the preferred crystallographic orientation of *c* axis alignment does not correspond to dominant slip by basal $\langle a \rangle$. Average values calculated for a burgers vector length of 6.37 Å typical for *f* slip, results in similar low values of 112 MPa. Such values would again suggest deformation dominated by GSS creep mechanism and are therefore rather unlikely. Assuming a burgers vector length of 8.09 Å we reach average differential stress values of around 142 MPa, plotting

SED
7, 2663–2695, 2015

close to the field boundary indicating that a high amount of dislocation activity might be active. The used burgers vector has been observed to operate during slip on *r* and *f* planes (Goetze and Kohlstedt, 1977). Assuming that the idea of rather cross slip being active than dislocation creep is valid, this Burgers vector seems to be the best fitting one. As already discussed the active slip system and therefore burgers vector is constantly changing due to rotation of calcite grains therefore the obtained stresses have to be considered with caution. Differential stresses calculated by the more recent experimental determined calibration suggested by de Bresser (1996) are almost identic with the ones calculated by paleowattmeter with an average of 197 MPa. The observation that stresses calculated by use of grain size and dislocation dependent calibrations seems to result in reliable almost identic values is indicating that no annealing occurred in the analysed ultramylonitic calcite after deformation. It is important to note that all calculated differential stresses lie below the threshold for brittle deformation determined from the Byerlee law (Byerlee, 1978) for suggested pressure conditions of around 200 and 400 MPa consistent with microstructural observation indicating that the deformation was ductile.

The deformation behaviour and strain rates predicted for the calculated stresses were examined by constructing a deformation mechanism map for calcite at 300 °C using calcite flow laws of Herwegh et al. (2003) and Renner et al. (2002). The average grain size has been plotted with respect to the corresponding differential stress calculated by paleowattmeter and paleopiezometer (Fig. 9) indicating strain rates of 10^{-9}–10^{-10} s^{-1}. The average grain size plots exactly at the boundary between GSS and grain size insensitive (GSI) creep consistent with the field boundary hypothesis (De Bresser et al., 1998, 2001), which is assumed to represent the balancing stable grain size between grain growth active during GSS creep and grain size reduction during GSI creep. Nevertheless the grain size range is relatively wide having a grain size between 1 and 9 µm and is therefore not at every point consistent with the field boundary.

SED
7, 2663–2695, 2015

5.3 Dislocation activity, texture development and GBS

The ultrafine-grained, equigranular microstructure of the Syros ultramylonite is characteristic of materials exhibiting GSS deformation (Eddington, 1976; Boullier and Guéguen, 1975; Schmid, 1976; Rutter, 1994). Grain size sensitivity results from the decreased diffusional mass transport distance through small grains (Nabarro–Herring creep), the enhanced diffusion rates through the integrated defects that are grain boundaries (Coble creep), and the reduced effective viscosity of grain boundaries that presents as independent GBS. Overall GSS flow reflects the role that grain boundaries play in accommodating very large macroscopic strains (Raj and Ashby, 1971; Ashby and Verrall, 1973; Gifkins, 1976, 1977; Langdon, 2009). GSS flow has in most materials, including rocks, been linked to a combination of low differential stress, sustained small grain size and homologous temperatures high enough to support diffusional accommodation of grain rearrangements during GBS (e.g. Ashby and Verrall, 1973; Boullier and Guéguen, 1975; Schmid, 1976). Only the small grain size is characteristic of the Syros ultramylonite.

GSS deformation mechanisms are anticipated to result in a randomization or loss in CPO intensity (Zhang et al., 1994; Bestmann and Prior, 2003; Storey and Prior, 2005) through grain boundary displacements and rotations (GBS) unrelated to intracrystalline deformation; however, a primary crystallographic texture forms in the ultramylonite (Fig. 5a).

A primary texture could in principle develop in one of three ways during GSS. Deformation within the GSS creep field is often associated with grain growth due to diffusion processes or surface energy driven coarsening (Aktinson, 1988). In a non-isotropic stress field the growth of grains during deformation will be stress directed and can result in a weak texture (Schmid et al., 1977; Bons and den Brok, 2000). The high deformation stress and strain rate conditions at relatively low temperatures appear to suppress any dominant crystal growth in the ultramylonite, with cyclic grain size reduction giving the relatively wide grain size range between 9 and 1 µm. The lack of

SED
7, 2663–2695, 2015

evidence for abundant grain growth makes stress directed growth a rather unlikely explanation for the observed texture.

A second explanation exists for the deformation of polyphase materials by diffusion (Coble) creep in combination with GBS where the development of a texture is due to reorientation of grains towards a preferred alignment for interface reactions (Heidelbach et al., 2000; Sundberg and Cooper, 2008). Deformation by GBS would be consistent with the observed random misorientation angle distribution (Fig. 5b) indicating that no relation between neighbouring grains exists, being a typical pattern observed for grains deformed by GBS (Wheeler et al., 2001; Bestmann and Prior, 2003). However, the ultramylonitic marble is essentially pure with only minor amounts of quartz, dolomite and mica, being stable over a wide range of P-T conditions along the P-T path of Syros (Rogowitz et al., 2015) making any mineral reactions almost impossible. Also the smooth surfaces of calcite grains argue against crystal growth and mineral reactions. This explanation can be dismissed.

Lastly, concomitant dislocation activity and GBS could create a texture. Schmid et al. (1977) deformed Solnhofen limestone at temperatures above 800 °C and Rutter et al. (1994), likewise, fine-grained calcite aggregates at temperatures around 700 °C for which they observed deformation of relict coarser grains by dislocation creep simultaneously with predominant GBS. The combination of dominant deformation by GBS and minor dislocation creep in grains that are too large to slide past each other, resulting in strain accommodation by grain boundary migration recrystallization, is a convenient explanation for observed curved grain boundaries of larger grains (Fig. 2c) and higher misorientations (up to 13°) in larger grains (Fig. 4c). Nevertheless, the latter are examples of dislocation activity of coarse grains within a fine matrix, not deformation of the matrix itself. In contrast to the latter cases, we observe extensive dislocation multiplication (Frank–Read sources) and high dislocation densities within small grains (Fig. 7), a microstructural combination that is distinct from the coarser calcite and demonstrates that the dislocations are not simply a late overprint pulse that intro-

SED
7, 2663–2695, 2015

duced dislocations in all part of the structure. Rather, a large amount of strain must be accommodated by crystal plasticity within small sliding grains.

Much of the discussion of GBS in rocks has focussed on diffusional accommodation in the style of Ashby and Verall (1973), although dislocation-accommodated GBS models (e.g. Crossman and Ashby, 1974; Gifkins, 1976, 1977) have been used to explain natural high strain deformation (White, 1982; Vitale et al., 2007). The introduction of high-strain torsion experiments has resolved the absence of characteristic microstructures and constitutive behaviour interpreted as dislocation-accommodated GBS (Hirth and Kohlstedt, 2003; Hansen et al., 2011; Kushnir et al., 2015).

The details of the accommodation process remain moot. Independent rotation and displacement of grains will in principle rotate the crystal orientation relative to the overall stress field providing for the activation of different dominant slip systems which could explain the intensity and various orientations of dislocations (Fig. 7). The absence of low-angle recovery boundaries and intracrystalline misorientation in fine-grained calcite from this study, and others (Vitale et al., 2007; Molli et al., 2011) excludes strain energy reduction by classical thermal activated dislocation creep still we observe strain softening rather than hardening in the ultramylonite. Observed networks and hexagonal cells, the 200 nm cells, might indicate activation of cross-slip (De Bresser and Spiers, 1990; Kennedy and White, 2002; Molli et al., 2011). Additional deformation by dislocation glide, being a fast strain energy reducing process, closes cavities by plastic deformation of a single crystal (Fig. 5e), resulting at the same time in the opening of new cavities at a different locality.

5.4 Origin of cavities and pores

The process of cavitation remains poorly understood. Proposed mechanisms for the nucleation of cavities in polycrystalline material include vacancy condensation at a high stress region, the presence of second particles, dislocation pile-up at grain boundaries and GBS (Kassner and Hayes, 2003; Ovid'ko and Sheinerman, 2006; Fusseis et al., 2009; Rybacki et al., 2010). The preferential location of grain boundary openings ori-

SED
7, 2663–2695, 2015

entated at a low angle to the shortening direction has already been observed by others in fine grained polycrystalline material (Ree, 1994; Mancktelow et al., 1998) and has been associated to the activity of GBS. Shape and location of cavities within the fine-grained ultramylonite is very similar to cavities described by Ree (1994) and Ovid'ko et al. (2011) as the result of grain neighbour switching during GBS. Opening of cavities occurs parallel to the shortening direction which are during further deformation partly closed due to further sliding of the grains, resulting in a small cavity at grain-triple junctions. Therefore, the observed grain boundary openings and cavities at four-grain and triple junctions (Figs. 3a–d and 5) are most likely related to GBS.

Small pores located on grain surfaces (Fig. 5e) are probably the result of minor grain boundary fluids or fluid filled pores (Mancktelow et al., 1998). The observed small cavities having the same orientation and piling up at grain boundaries (Figs. 3g and h and 5f) might be interpreted as Zener–Stroh cracks, being the result of stress concentration due to dislocation pile-up at grain boundaries (Stroh, 1954, 1955; Fan and Xiao, 1997). Due to movement of edge dislocations on the same slip plane the uniform orientation of cracks can be explained. Another possible explanation is stress concentration at obstacles or ledges at grain boundaries. Such features can result in stress concentration during grain sliding and lead to microcracking (Chan et al., 1986).

6 Conclusions

1. Detailed microstructural analysis of a highly strained ($80 < \gamma < 1000$) calcite ultramylonite shows that at strain rates on the order of 10^{-9}–10^{-10} s^{-1} recrystallization by bulging results in strain free, small grains.

2. The reduction in grain size results in deformation by GBS. Due to high stress and strain rate conditions at low temperatures and dry conditions in a stable mineral paragenesis, dislocation activity is principal deformation mechanism accommodating strain compatability between sliding grains.

SED
7, 2663–2695, 2015

3. The absence of characteristic dislocation creep features such as low angle grain boundaries and intracrystalline misorientation, together with the presence of dislocation glide networks and parallel traces of dislocations indicates that cross slip and network assisted dislocation movement aid in low-temperature recovery of the deforming calcite, given the inadequacy of thermal-induced recovery (climb) to reduce strain hardening effects.

4. Consistency of stresses calculated by grain size and dislocation density dependent calibrations resulting in stresses of around 190 MPa indicates that no annealing occurred.

5. The switch from dislocation creep to simultaneous activation of GBS and dislocation activity results in extreme strain softening and can be an important strain localization process in calcite rocks, even at high strain rate ($\sim 10^{-9}\,s^{-1}$) and low temperature (300 °C), where brittle deformation could be anticipated. Such transitions in ultrafine-grained monomineralic rocks provide an example of the inverse Hall–Petch relationship at low temperature where below a critical grain size, the active deformation micromechanisms transition to a lower flow stress (e.g. Carlton and Ferreira, 2007).

The Supplement related to this article is available online at doi:10.5194/sed-7-2663-2015-supplement.

Acknowledgements. We thank the University of Vienna (grant number IK543002) for supporting the doctoral school DOGMA, the Austrian Science Fund (FWF): I471-N19 and the Natural Sciences and Engineering Research Council of Canada for a Discovery Grant (Fracture, Friction and Flow). We would like to thank Gerlinde Habler for FIB foil preparation and the University of New Brunswick Microscopy and Microanalysis Facility, particularly Louise Weaver, for support during TEM work. Many thanks to Luiz Morales, Luca Menegon and Benjamin Huet for valuable discussions.

SED
7, 2663–2695, 2015

References

Ashby, M. F. and Verrall, R. A.: Diffusion-accommodated flow and superplasticity, Acta Metall. Mater., 21, 149–163, 1973.

Atkinson, H. V.: Theories of normal grain growth in pure single phase systems, Acta Metall. Mater., 36, 469–491, 1988.

Austin, N. and Evans, B.: The kinetics of microstructural evolution during deformation of calcite, J. Geophys. Res., 114, B09402, doi:10.1029/2008JB006138, 2009.

Bachmann, F., Hielscher, R., and Schaeben, H.: Texture analysis with MTEX – free and open source software toolbox, Sol. St. Phen., 160, 63–68, 2010.

Bestmann, M. and Prior, D. J.: Intragranular dynamic recrystallization in naturally deformed calcite marble: diffusion accommodated grain boundary sliding as a result of subgrain rotation recrystallization, J. Struct. Geol., 25, 1597–1613, 2003.

Blenkinsop, T. G.: Cataclasis and processes of particle size reduction, Pageoph., 136, 59–86, 1991.

Bons, P. D. and den Brok, B.: Crystallographic preferred orientation development by dissolution-precipitation creep, J. Struct. Geol., 22, 1713–1722, 2000.

Boullier, A. M. and Guéguen, Y.: SP-mylonites: origin of some mylonites by superplastic flow, Contrib. Mineral. Petr., 50, 93–104, 1975.

Bunge, H. J.: Texture Analysis in Materials Science: Mathematical Models, Butterworths, London, 1982.

Byerlee, J. D.: Friction of rock, Pure Appl. Geophys., 116, 615–626, 1978.

Carlton, C. E. and Ferreira, P. J.: What is behind the inverse Hall–Petch effect in nanocrystalline materials?, Acta Mater., 55, 3749–3756, 2007.

Chan, K. S., Page, R. A., and Lankford, J.: Cavity nucleation at grain boundary ledges, Acta Metall. Mater., 34, 2361–2370, 1986.

Crossmanm, F. W. and Ashby, M. F.: The non-uniform flow of polycrystals by grain boundary sliding accommodated by power-law creep, Acta Metall. Mater., 23, 425–440, 1975.

Dandekar, D. P.: Variation in the elastic constants of calcite with temperature, J. Appl. Phys., 39, 3694–3699, 1968.

De Bresser, J. H. P.: Steady state dislocation densities in experimentally deformed calcite materials: single crystal vs. polycrystals, J. Geophys. Res., 101, 189–201, 1996.

SED
7, 2663–2695, 2015

De Bresser, J. H. P. and Spiers, C. J.: High temperature deformation of calcite single crystals by r+ and f+ slip, deformation mechanisms, rheology and tectonics, Geological Society London Special Publications, 54, 285–298, 1990.
De Bresser, J. H. P., Peach, C. J., Reijs, J. P. J., and Spiers, C. J.: On dynamic recrystallization during solid state flow: effects of stress and temperature, Geophys. Res. Lett., 25, 3457–3460, 1998.
De Bresser, J. H. P., Ter Heege, J., and Spiers, C.: Grain size reduction by dynamic recrystallization: Can it result in major rheological weakening?, Int. J. Earth Sci., 90, 28–45, 2001.
Etherdige, M. A. and Wilkie, J. C.: Grain size reduction, grain boundary sliding and flow strength of mylonites, Tectonophysics, 58, 159–178, 1979.
Fan, H. and Xiao, Z. M.: A Zener–Stroh Crack near an interface, Int. J. Solids Struct., 34, 2829–2842, 1997.
Fusseis, F., Regenauer-Lieb, K., Liu, J., Hugh, R. M., and De Carlo, F.: Creep cavitation can establish a dynamic granular fluid pump in ductile shear zones, Nature, 459, 974–977, doi:10.1038/nature08051, 2009.
Gifkins, R. C.: Grain-boundary sliding and its accommodation during creep and superplasticity, Metall. Trans. A, 7, 1225–1232, 1976.
Goetze, C. and Kohlstedt, D. L.: The dislocation structure of experimentally deformed marble, Contrib. Mineral. Petr., 59, 293–306, 1977.
Grasemann, B. and Stüwe, K.: The development of flanking folds during simple shear and their use as kinematic indicators, J. Struct. Geol., 23, 715–724, 2001.
Hansen, L. N., Zimmerman, M. E., and Kohlstedt, D. L.: Grain boundary sliding in San Carlos olivine: flow law parameters and crystallographic preferred orientation, J. Geophys. Res., 116, B08201, doi:10.1029/2011JB008220, 2011.
Hardwick, D., Sellars, C. M., and Tegart, W. J.: Structural changes during the deformation of copper, aluminium and nickel at high temperatures and high strain rates, J. I. Met., 90, 17–22, 1961.
Heidelbach, F., Post, A., and Tullis, J.: Crystallographic preferred orientation in albite samples deformed experimentally by dislocation and solution precipitation creep, J. Struct. Geol., 22, 1649–1661, 2000.
Herwegh, M., Xiao, X., and Evans, B.: The effect of dissolved magnesium on diffusion creep in calcite, Earth Planet. Sc. Lett., 212, 457–470, 2003.

SED
7, 2663–2695, 2015

Hirth, G. and Kohlstedt, D. L.: Rheology of the upper mantle and the mantle wedge: a view from the experimentalists, in inside the subduction factory, Geoph. Monog. Series, 138, 83–105, 2003.
Jolivet, L. and Brun, J. P.: Cenozoic geodynamic evolution of the Aegean, Int. J. Earth Sci., 99, 109–138, 2010.
Kassner, M. E. and Hayes, T. A.: Creep cavitation in metals, Int. J. Plasticity, 19, 1715–1748, 2003.
Keiter, M., Piepjohn, K., Ballhaus, C., Lagos, M., and Bode, M.: Structural development of high-pressure metamorphic rocks on Syros island (Cyclades, Greece), J. Struct. Geol., 26, 1433–1445, 2004.
Kennedy, L. A. and White, J. C.: Low-temperature recrystallization in calcite: mechanisms and consequences, Geology, 29, 1027–1030, 2001.
Kohlstedt, D. L. and Weathers, M. S.: Deformation induced microstructures, paleopiezometers and differential stresses in deeply eroded fault zones, J. Geophys. Res., 85, 6269–6285, 1980.
Kushnir, A. R. L., Kennedy, L. A., Misra, S., Benson, P., and White, J. C.: The mechanical and microstructural behaviour of calcite-dolomite composites: an experimental investigation, J. Struct. Geol., 70, 200–216, 2015.
Langdon, T. G.: Seventy-five years of superplasticity: historic developments and new opportunities, J. Mater. Sci., 44, 5998–6010, 2009.
Mackenzie, J. K. and Thompson, M. J.: Some statistics associated with the random disorientation of cubes, Biometrika, 44, 205–210, 1957.
Mair, K. and Abe, S.: Breaking up: comminution mechanisms in sheared simulated fault gouge, Pure Appl. Geophys., 168, 2277–2288, 2011.
Mancktelow, N. S., Grujic, D., and Johnson, E. L.: An SEM study of porosity and grain boundary microstructure in quartz mylonites, Simplon Fault Zone, Contrib. Mineral. Petr., 131, 71–85, 1998.
Menegon, L., Stünitz, H., Nasipuri, P., Heilbronner, R., and Svahnberg, H.: Transition from fracturing to viscous flow in granulite facies perthitic feldspar (Lofoten, Norway), J. Struct. Geol., 48, 95–112, 2013.
Molli, G., White, J. C., Kennedy, L., and Taini, V.: Low-temperature deformation of limestone, Isola Palmaria, northern Apennine, Italy – the role of primary textures, precursory veins and intracrystalline deformation in localization, J. Struct. Geol., 33, 255–270, 2011.

SED
7, 2663–2695, 2015

Ovid'ko, I. A. and Sheinerman, A. G.: Nanovoid generation due to intergrain sliding in nanocrystalline materials, Philos. Mag., 86, 3487–3502, 2006.
Ovid'ko, I. A., Sheinerman, A. G., and Skiba, N. V.: Elongated nanoscale voids at deformed special grain boundary structures in nanocrystalline materials, Acta Mater., 59, 678–685, 2011.
Papanikolaou, D. J.: Tectonic evolution of the Cycladic Blueschist Belt (Aegean Sea, Greece), in: Chemical Transport in Metasomatic Processes, edited by: Helgeson, H. C., Springer, the Netherlands, 429–450, 1987.
Passchier, C.: Flanking structures, J. Struct. Geol., 23, 951–962, 2001.
Pennacchioni, G. and Mancktelow, N. S.: Nucleation and initial growth of a shear zone network within compositionally and structurally heterogeneous granitoids under amphibolite facies conditions, J. Struct. Geol., 29, 1757–1780, 2007.
Philippon, M., Brun, J. P., and Gueydan, F.: Tectonics of the Syros blueschists (Cyclades, Greece): from subduction to Aegean extension, Tectonics, 30, TC4001, doi:10.1029/2010TC002810, 2011.
Platt, J. P. and Behr, W. M.: Grainsize evolution in ductile shear zones: implications for strain localization and the strength of the lithosphere, J. Struct. Geol., 33, 537–550, 2011.
Poirier, J. P. and Nicolas, A.: Deformation-induced recrystallization due to progressive misorientation of subgrains, with special reference to mantle peridotites, J. Geol., 83, 707–720, 1975.
Raj, R. and Ashby, M. F.: On grain boundary sliding and diffusional creep, Metall. Trans., 2, 1113–1127, 1971.
Ree, J. H.: Grain boundary sliding and development of grain boundary openings in experimentally deformed octachloropropane, J. Struct. Geol., 16, 403–418, 1994.
Renner, J., Evans, B., and Siddiqi, G.: Dislocation creep of calcite, J. Geophys. Res., 107, ECV6-1–ECV6-16, 2002.
Rogowitz, A., Grasemann, B., Huet, B., and Habler, G.: Strain rate dependent calcite microfabric evolution – An experiment carried out by nature, J. Struct. Geol., 69, Part A, 1–17, 2014.
Rogowitz, A., Huet, B., Schneider, D., and Grasemann, B.: Influence of high strain rate deformation on $^{40}Ar/^{39}Ar$ mica ages from marble mylonites (Syros, Greece), Lithosphere, L455.1, doi:10.1130/L455.1, 2015.

SED
7, 2663–2695, 2015

Rutter, E. H., Casey, M., and Burlini, L.: Preferred crystallographic orientation development during the plastic and superplastic flow of calcite rocks, J. Struct. Geol., 16, 1431–1446, 1994.
Rybacki, E., Wirth, R., and Dresen, G.: Superplasticity and ductile fracture of synthetic feldspar deformed to large strain, J. Geophys. Res., 115, B08209, doi:10.1029/2009JB007203, 2010.
Sakai, T. and Jonas, J. J.: Overview no. 35 dynamic recrystallization: mechanical and microstructural considerations, Acta Metall. Mater., 32, 189–209, 1984.
Sakai, T., Belyakov, A., Kaibyshev, R., Miura, H., and Jonas, J. J.: Dynamic and post-dynamic recrystallization under hot, cold and severe plastic deformation conditions, Prog. Mater. Sci., 60, 130–207, 2014.
Schmid, S. M.: Rheological evidence for changes in the deformation mechanism of Solnhofen limestone towards low stress, Tectonophysics, 31, T21–T28, 1976.
Schmid, S. M., Boland, J. N., and Paterson, M. S.: Superplastic flow in fine grained limestone, Tectonophysics, 43, 257–291, 1977.
Schmid, S. M., Paterson, M. S., and Boland, J. N.: High temperature flow and dynamic recrystallization in Carrara marble, Tectonophysics, 65, 245–280, 1980.
Schumacher, J. C., Brady, J. B., Cheney, J. T., and Tonnsen, R. R.: Glaucophane-bearing marbles on Syros, Greece, J. Petrol., 49, 1667–1686, 2008.
Segall, P. and Pollard, D. D.: Joint formation in the granitic rock of the Sierra Nevada, Bull. Geol. Soc., 94, 563–575, 1983.
Sundberg, M. and Cooper, R. F.: Crystallographic preferred orientation produced by diffusional creep of harzburgite: effects of chemical interactions among phases during plastic flow, J. Geophys. Res.-Sol. Ea., 113, B12208, doi:10.1029/2008JB005618, 2008.
Stroh, A. N.: The Formation of Cracks as a Result of Plastic Flow, The Royal Society of London, Series A, doi:10.1098/rspa.1954.0124, 1954.
Stroh, A. N.: The Formation of Cracks as a Result of Plastic Flow II, The Royal Society of London, Series A, doi:10.1098/rspa.1955.0238, 1955.
Storey, C. D. and Prior, D. J.: Plastic deformation and recrystallization of garnet: a mechanism to facilitate diffusion creep, J. Petrol., 46, 2593–2613, 2005.
Takeuchi, S. and Argon, A. S.: Steady-state creep of single phase crystalline material at high temperature, J. Mater. Sci., 11, 1542–1566, 1976.
Trotet, F., Vidal, O., and Jolivet, L.: Exhumation of Syros and Sifnos metamorphic rocks (Cyclades, Greece). New constraints on the P-T paths, Eur. J. Mineral., 13, 901–920, 2001.

SED
7, 2663–2695, 2015

Vitale, S., White, J. C., Iannace, A., and Mazzoli, S.: Ductile strain partitioning in micritic limestones, Calabria, Italy: the roles and mechanisms of intracrystalline and intercrystalline deformation, Can. J. Earth Sci., 44, 1587–1602, 2007.
Wang, Z., Zhao, Y., and Kohlstedt, D. L.: Dislocation creep accommodated by grain boundary sliding in dunite, J. Earth Sci., 21, 541–554, 2010.
Wheeler, J., Prior, D., Jiang, Z., Spiess, R., and Trimby, P.: The petrological significance of misorientations between grains, Contrib. Mineral. Petr., 141, 109–124, 2001.
White, J. C.: Quartz deformation and the recognition of recrystallization regimes in the Flinton Group conglomerates, Ontario, Can. J. Earth Sci., 19, 81–93, 1982.
White, J. C. and White, S. H.: High-voltage transmission electron microscopy of naturally deformed polycrystalline dolomite, Tectonophysics, 66, 35–54, 1980.
White, J. C. and White, S. H.: On the structure of grain boundaries in tectonites, Tectonophysics, 78, 613–628, 1981.
White, S.: Syntectonic recrystallization and texture development in quartz, Nature, 244, 276–278, 1973.
White, S.: Geological significance of recovery and recrystallization processes in quartz, Tectonophysics, 39, 143–170, 1977.
White, S. H., Burrows, S. E., Carreras, J., Shaw, N. D., and Humphreys, F. J.: On mylonites in ductile shear zones, J. Struct. Geol., 2, 175–187, 1980.
Wortel, M. J. R., Goes, S. D. B., and Spakman, W.: Structure and seismicity of the Aegean subduction zone, Terra Nova, 2, 554–562, 1993.
Zhang, Y., Hobbs, B. E., and Jessell, M. W.: The effect of grainboundary sliding on fabric development in polycrystalline aggregates, J. Struct. Geol., 16, 1315–1325, 1994.

SED
7, 2663–2695, 2015

Figure 1. (a) Image presenting the studied flanking structure on Syros. The red line traces the crosscutting element (i.e. shear zone). **(b)** Close-up of the boundary between the shear zone (SZ) and host rock (HR) showing thin porcelain like layer (UFG).

SED
7, 2663–2695, 2015

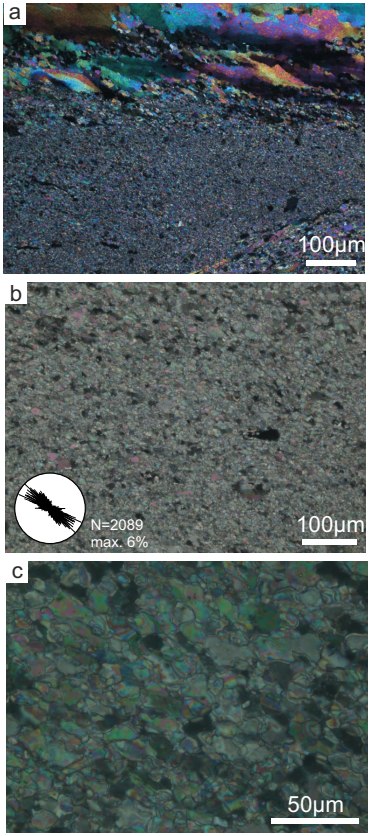

Figure 2. Optical micrographs of calcite marble (crossed polarizers). **(a)** Transition between host rock and fine-grained ultramylonite. Note the extreme grain size reduction. **(b)** Fine almost equigranular ultramylonite. The inserted sketch represents a rose-diagram showing the 2-D-orientation of long axis of calcite grains. **(c)** Close-up of fine-grained ultramylonite. Note that grain boundaries of coarser grains are strongly curved compared to smaller grains.

SED
7, 2663–2695, 2015

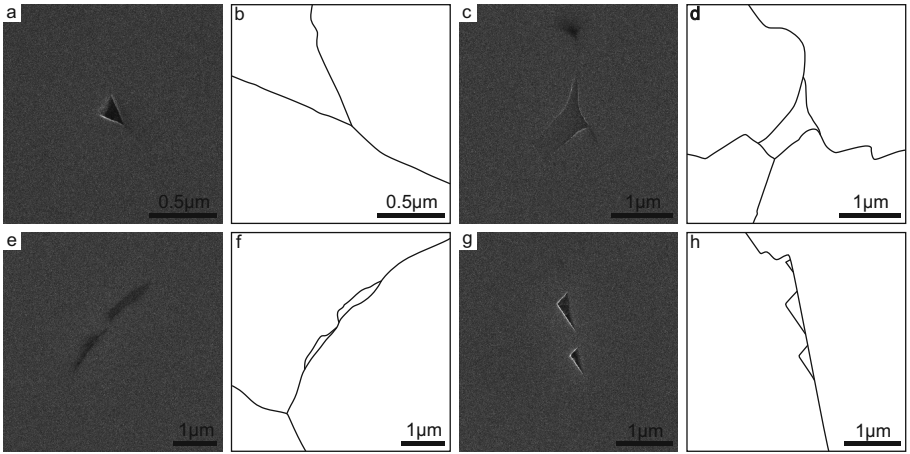

Figure 3. Secondary electron images showing preferred locality of cavities in fine-grained ultramylonite **(a, c, e, g)**. The sketches represent grain boundary drawings of the areas respectively **(b, d, f, h)**. **(a, b)** Small cavity at grain boundary triple junction. **(c, d)** Cavity located at four-grain junction. **(e, f)** Grain boundary opening at grain boundary in extension. **(g, h)** Zener–Stroh cracks due to dislocation pile up at the grain boundary. Note that the three small cracks show the same orientation.

SED
7, 2663–2695, 2015

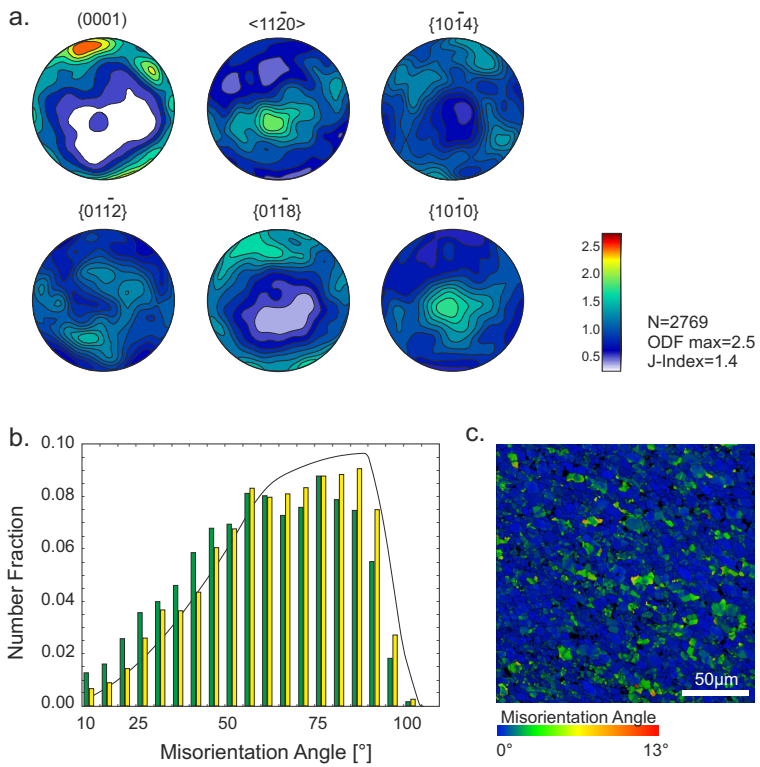

Figure 4. (a) Stereographic equal area lower hemisphere projection of *c* (0001) and – *a* ⟨11-20⟩ axes and poles of *r* {10-41}, *f* {01-12}, *e* {01-18} and *m* {10-10} planes. *N* represents the number of analyzed grains. Texture strength is represented by the intensity of the orientation distribution function (ODF), additionally information on *J* index are given. **(b)** Histogram showing the misorientation angle distribution of neighbor-pair (green) and random-pair grains (yellow). The curve represents the calculated theoretical curve for a perfectly random misorientation angle distribution for trigonal crystal symmetry. **(c)** Orientation deviation map representing the misorientation over each grain with respect to its average misorientation.

SED
7, 2663–2695, 2015

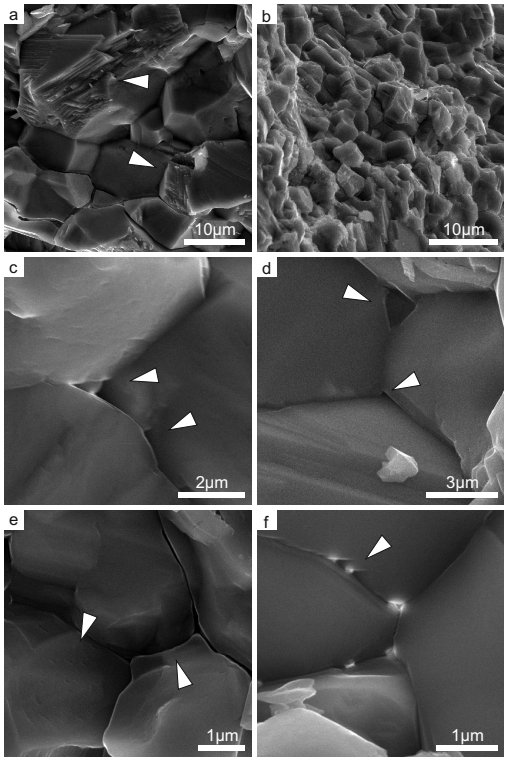

Figure 5. SE images of broken specimens. **(a)** Slightly coarser grained area showing how grains larger 15 µm break along the cleavage while small grains break along their boundaries. **(b)** Fine equigranular calcite grains showing crystal faces. **(c)** Small cavities at grain triple junctions and grain boundaries next to ledges. **(d)** Cavities at grain triple junctions. **(e)** Grain boundary openings appearing to be closed by flowing grain. Note the small pores on the grain surface of the left grain. **(f)** Small cavities having the same orientation piling up at the grain boundary.

SED
7, 2663–2695, 2015

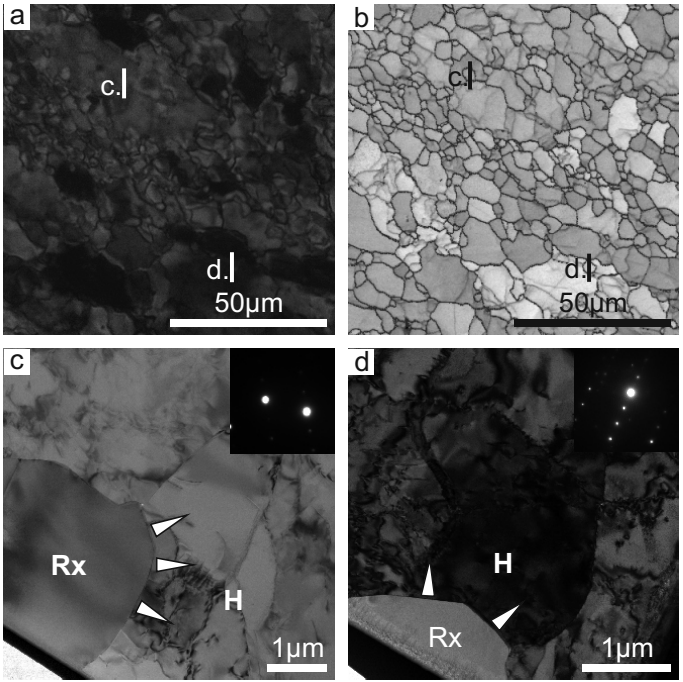

Figure 6. (a) Optical micrograph (crossed polarizer) showing the transition zone between coarse and fine- grained ultramylonite. **(c, d)** represent the locality of focused ion beam (FIB) foils. **(b)** Electron backscatter diffraction (EBSD) map showing transition zone between coarse and fine grained ultramylonite. High angle boundaries (> 15°) are plotted in blue. **(c, d)** show the locality of FIB foils. Note that the foils represent a profile across fine grained ultramylonitic grains adjacent to a coarse grain. **(c)** Dislocation-rich host (*H*) calcite and dislocation-free recrystallized (Rx) grains. Bulging (migration) direction of recrystallizing grain boundary shown by arrows. TEM Bright field; g = 02-2-1. **(d)** Dislocation-free calcite grain (Rx) adjacent to coarser grains with a high density of free dislocations and dislocations arranged to low-angle grain boundaries. Bright field TEM; $B \sim$ [2-201] in host grain.

SED
7, 2663–2695, 2015

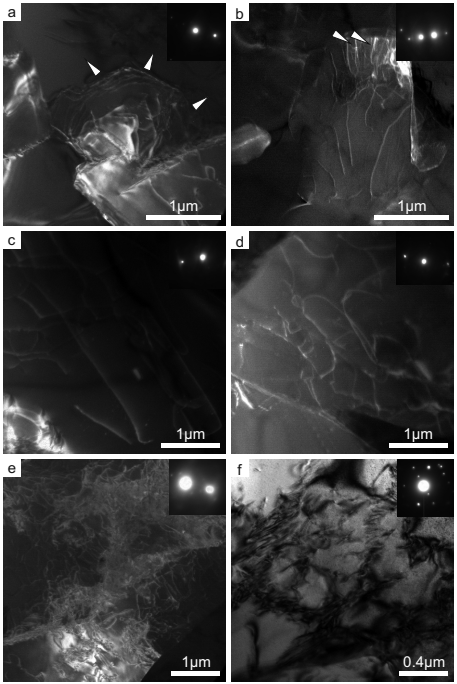

Figure 7. Typical TEM dislocation structures within the fine-grained ultramylonite. **(a)** Frank–Read source pinned at a grain boundary with multiplication and propagation of dislocation loops outward (arrows) on a *f* {01-12} glide plane; TEM Dark field, g = 12–35. **(b)** Glide dislocations pinned at a grain boundary (arrows); TEM Bright field, g = 0–114. **(c)** Extended glide dislocations. TEM Dark field; g = 31–42. **(d)** Dislocation gliding in *f* plane with notable dipole (arrow). TEM Dark field; g = 1-32-4. **(e)** Typical high dislocation density in UFG calcite. TEM Dark field; g = 30–33. **(f)** Cells ("200 nm" structure) defined by dislocation arrays interpreted to be related to network-assisted recovery at low homologous temperature. TEM Bright field; $B \sim$ [2-1-10] g = 0–114.

SED
7, 2663–2695, 2015

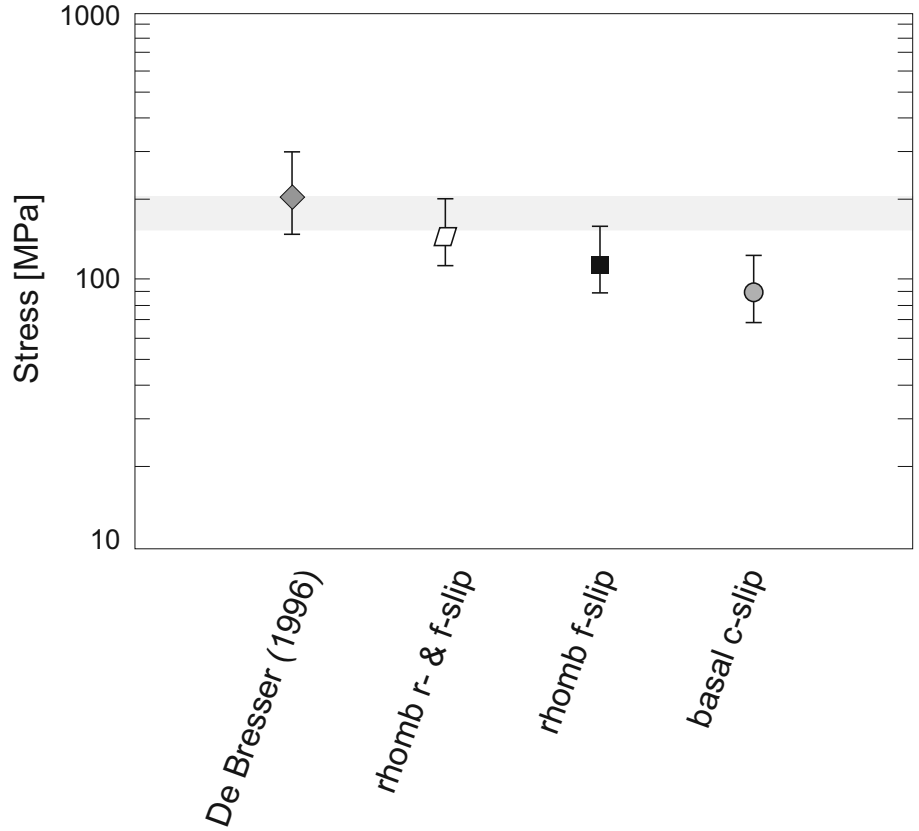

Figure 8. Logarithmic plot showing the calculated average stress values for the different used equations and glide systems. The bars represent the stress range for an average dislocation density. Gray shaded area displays the calculated stress by paleowattmeter (Austin and Evans, 2009) and paleopiezometer (Schmid et al., 1980).

SED
7, 2663–2695, 2015

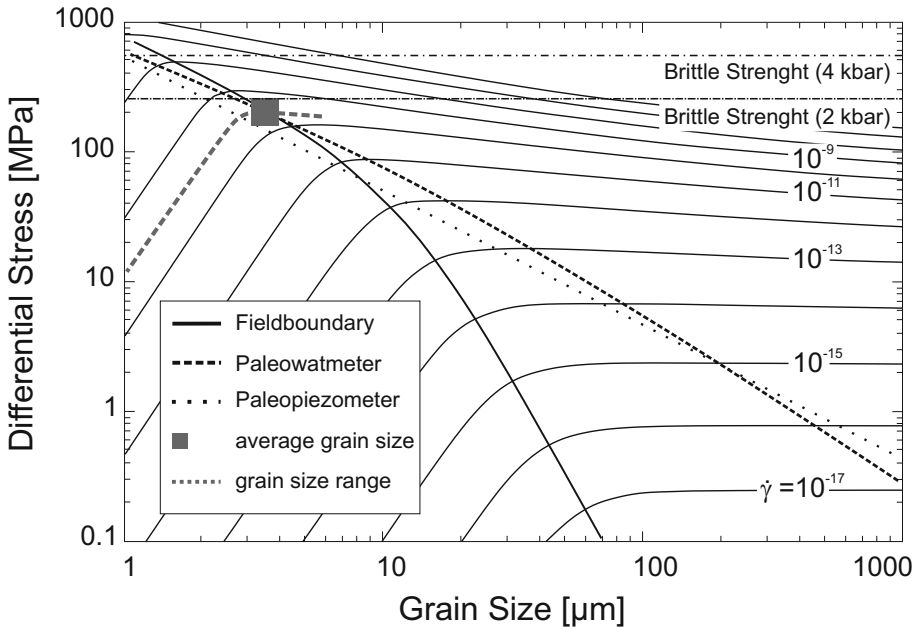

Figure 9. Deformation mechanism map for calcite at 300 ˚C in the differential stress vs. grain size space. Used flow laws are by Renner et al. (2002) for the dislocation creep field and Herwegh et al. (2003) for grain size sensitive creep. Additionally paleowattmeter (Austin and Evans, 2009), paleopiezometer (Schmid et al., 1980), the field boundary after De Bresser et al. (1998, 2001) and the brittle strength (Byerlee, 1978) are plotted. The rectangle represents the average grain size.

SED
7, 2663–2695, 2015